1
Advances in Blister-Actuated Laser Induced Forward Transfer (BA-LIFT)

Blister-actuated laser-induced forward transfer (BA-LIFT) is a laser printing technique that enables the deposition of liquids droplets with lateral resolution down to a few micrometers. BA-LIFT was developed to overcome some of the limitations of classical LIFT by enabling the transfer of sensitive materials, such as functional polymers and molecules, biomolecules, and living organisms while retaining their functionality intact. BA-LIFT utilizes a laser pulse that is absorbed in a thick polymer layer, which undergoes plastic deformation and forms a rapidly expanding blister. With an ink layer coating the polymer layer, this blister expansion provides the impulse for jet formation and ultimately material transfer. BA-LIFT is different compared to other conventional LIFT processes because the ink itself is not directly exposed to the laser, either optically or thermally during this process due to the thickness of the polymer layer. The jet is formed purely due to mechanical deformation, making sure that the chemical composition of the ink remains intact and undisturbed. As a result, this strategy has great potential for the transfer of delicate materials and can be used in bio-related applications and organic electronics. This chapter aims to explain the developments in the BA-LIFT process. Time-resolved imaging studies are presented along with the advances in the modeling of the BA-LIFT.

Contents

1 Advances in Blister-Actuated Laser Induced Forward Transfer (BA-LIFT) *1*
1.1 Introduction *3*
1.2 BA-LIFT Basics *5*
1.3 Why BA-LIFT? *6*
1.4 Blister Formation *8*
1.4.1 Dynamics of Blister Formation *8*
1.4.2 Finite Element Modeling of Blister Formation *12*
1.5 Jet Formation and Expansion *16*
1.5.1 Computational Fluid Dynamics Model *16*
1.5.2 Effect of the Laser Energy *18*
1.5.3 Effect of the Ink Film Properties *20*
1.6 Application to the Transfer of Delicate Materials *24*
1.7 Conclusions *27*

1.1 Introduction

Laser-induced forward transfer (LIFT) is a laser printing technique that enables the simultaneous transfer and patterning of material from a donor to an acceptor substrate with a lateral resolution down to a few micrometers [1, 2]. As described in many chapters in this book, this technique has been used in various solid or liquid printing applications ranging from organic biomaterials [3, 4, 5, 6] to metals [7, 8, 9]. In the case of liquid LIFT, transfer is initiated in the form of a liquid jet that draws liquid from the donor film onto the acceptor substrate. The coupling of the laser energy into the liquid, also called *ink*, is therefore a critical part of the process. Conventional LIFT techniques employ two distinct mechanisms for that purpose: the first one relies on the absorption of the laser pulse directly into the ink, and is called direct-matrix absorption (DMA). The other technique uses a dynamic release layer (DRL) to absorb the laser energy. There are numerous studies published that compare both techniques with different inks and DRL materials [10, 11, 12]. However, for many sensitive materials, direct exposure to the laser beam or to the heat associated with

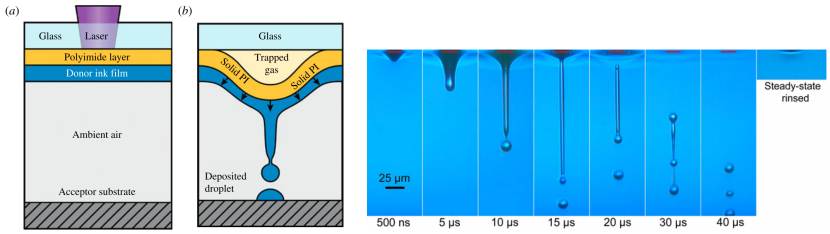


Figure 1.1 Left: Laser-induced forward transfer utilizing a polymer laser-absorbing layer: (a) the laser is absorbed within a thin layer of the polymer film, (b) ablating a confined pocket of gas and forcing the remaining film away from the glass as a rapidly expanding blister. If the impulse provided by the blister is sufficient, a small volume of ink is ejected onto an acceptor substrate [15]. Right: Transfers from a 10 μm film of NMP spread on 6 μm polyimide film initiated with a 20 μm beam at 1.3 J/cm^2 fluence. The vertical field of view is 200 μm and the bars indicate the beam size and location [16].

laser absorption leads to unacceptable damages. Using a metal DRL does shield the ink from laser radiation, but not from heat. In addition, ablated metal particles can contaminate the ink, which is unacceptable in particular applications. Polymer DRLs, such as triazene polymer, offer an alternative to the contamination issue, but the vaporization of the thin layer still has the potential to damage the most sensitive materials. Blister-actuated LIFT (BA-LIFT) has been developed to mitigate these issues by fully isolating the transfer liquid from the light and heat of the laser beam, and from contamination of ablation products. These concerns are adressed in literature [11], and it is shown according to nuclear magnetic resonance (NMR) spectroscopy and photoluminescence studies that BA-LIFT preserves the integrity of sensitive inks where the other techniques can be damaging [13].

BA-LIFT distinguishes itself from other liquid LIFT technique by the use of a relatively thick ($\sim 1 - 10\mu m$) polymer layer between the ink and the transparent substrate, which absorbs the laser. Upon ablation of a portion of the polymer film, the expansion of trapped gasses results in a blister on the polymer layer. This polymer blister fulfills two purposes: it converts the laser and chemical energy released during laser ablation into a mechanical impulse that propels the ink. It also fully shields the ink from laser light, heat, and contamination by ablation products. The comparison of BA-LIFT with other conventional LIFT techniques is presented in [14]. There it is shown that BA-LIFT preserves the integrity of termally and mechanically sensitive luminophores, whereas DMA and DRL techniques result in the degradation of the chemical integrity of these substances.

The mechanism for BA-LIFT along with an example are presented in Figure 1.1. The distinct feature of BA-LIFT, the presence of a relatively thick polymer layer (polyimide) between the glass slide and the donor ink film, is represented in yellow on Figure 1.1 (a-b). A blister is created upon irradiation with a UV laser pulse, which creates the impulse to drive the donor ink film (shown in blue) into a jet. The right hand side of Figure 1.1 shows the evolution of this jet as a time sequence taken by

pump-probe microscopy [16].

In summary BA-LIFT offers a platfom to print liquids and suspensions by relying on the the mechanical impulse created through the rapid expansion of a thin polymer layer. In BA-LIFT, direct laser-ink interaction is prevented with the utilization of the polymer layer. The details and applications of this process are given in this chapter. The experimental setup for BA-LIFT is very similar to setups for the conventional LIFT experiment. The details on polymer layer deposition and the experimental methods are given in Section 1.2. Time-resolved imaging of the BA-LIFT jetting is presented in Section 1.3. Blister formation on polymer layers is investigated extensively and details of this process can be found in Section 1.4. Jet formation during BA-LIFT is investigated using computational fluid dynamics (CFD). The modeling effort is presented in Section 1.5. BA-LIFT is used to transfer delicate materials while not disrupting the chemical integrity of the inks. An application for this is presented in Section 1.6. The chapter ends with the concluding remarks and directions for future work in Section 1.7.

1.2 BA-LIFT Basics

BA-LIFT works by the rapid creation of a blister from a polymer layer. The ideal polymer should strongly absorb the laser pulse within a short depth, undergo clean and efficient ablation and deform plastically without rupturing. Additionally, this polymer should not dissolve in any solvent composing the ink. This last condition is also known as *solvent orthogonality*. One common polymer that satisfies all these criteria is polyimide [17]. Polyimide has the advantage of being among the most studied polymers for laser ablation and its properties are well documented in the literature[17, 18, 19].

A polymer layer can be created by spin coating onto a glass microscope slides at various speeds to control layer thickness. In the specific case of polyimide, a precursor solution is applied and subsequent thermal processing is used to drive out excess solvent and complete the imidization process. [16, 12, 15, 20] After imidization and cross linking, polyimide becomes practically insoluble, and is therefore an ideal substrate on which to coat water-based and organic inks.

The laser used in the studies presented in this chapter is primarily a frequency-tripled Nd:YVO_4 laser, which has a wavelength of $\lambda = 355$ nm and a pulse duration of $\tau = 20$ ns, however other lasers wavelengths and pulse durations can be used provided they are absorbed in the polymer film leading to ablation of the material. Laser irradiation of polyimide with a nanosecond UV laser pulse results in decomposition of the polymer into fragments, notably gaseous species (CO, CO_2, HCN, and C_2H_2) [21, 22]. In the case of free-surface ablation, the ablation products are ejected from the surface under the action of the gas pressure. However in the case of BA-LIFT, the rapid creation of ablated species confined between the intact portion of the film and the glass substrate leads to the build up of pressure which is released though the deformation of the remaining polyimide film into a blister. In order to achieve a

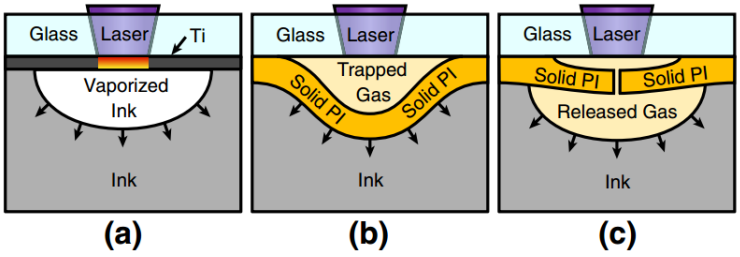


Figure 1.2 Mechanisms for laser-induced actuation of flow within the ink film [12]. (a) Laser absorption within a Ti film that results in vaporization of the solvents in adjacent ink, (b) Laser absorption within a PI layer produces an expanding, sealed blister, (c) Laser absorption within a PI layer causes its rupture and releases high-pressure gases.

proper blister it is crucial that only a part of the film is ablated while the remaining layer stays intact. This *partial* ablation occurs when the penetration depth of the laser into the material, or more importantly the effective ablation depth, is smaller than the total thickness of the film.

For the experiments shown here, the thickness of the polyimide film is typically 3.5–7 μm, whereas the penetration or absorption depth, at which the incident intensity has dropped to 1/e, is $d = 1/\alpha = 0.37$ μm. After 0.85 μm, the incident intensity has dropped to 10% of its inital value, which is well below the film thickness. The absorption depth allows us to estimate the residual intensity that is transmitted through the film. However, the absorption depth is not a good metric for the actual ablation depth [18]. In addition, the absorption process and optical reflection from the confined ablation plume makes it difficult to model blister expansion for a given laser energy [23]. Therefore, experiments are critical for obatining the specific details of blister formation and expansion.

1.3 Why BA-LIFT?

To appreciate the fundamental differences among different LIFT processes, it is instructive to perform time-resolved imaging [12]. In this study, we explored three different cases as described in Figure 1.2. The first case deals with a traditional titanium DRL layer, BA-LIFT is the second case and the third case represents BA-LIFT where the blister ruptures due to excessive incident laser energy.

Time-resolved imaging studies require a 100 ns resolution to accurately capture the dynamics of the blister expansion and jet formation. Pump-probe imaging is performed by taking a single snapshot of a jet at particular time, and shifting the delay between the pump and the probe to capture the whole sequence. All the BA-LIFT studies used a nanosecond flash lamp or diode along with a charge-coupled device (CCD) camera connected to a delay generator and synchronized with the laser pulse.

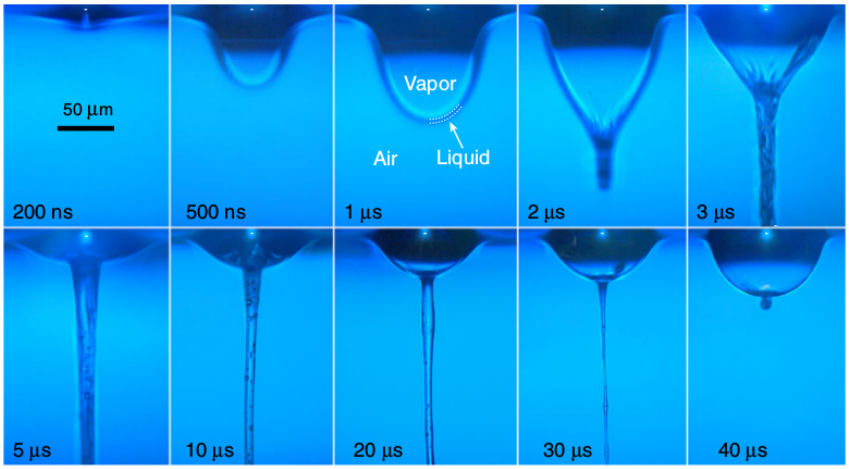


Figure 1.3 Time-resolved images of liquid ejection into the ambient air using a 50-nm titanium absorbing layer. A 1.6-μJ laser pulse is focused into the titanium film to a spot size of 2.5 μm (indicated by a white marker), initiating liquid ejection from an adjacent 5-μm film [12]. Fluid motion is initiated by focusing a 1.6 μJ laser pulse into the titanium layer to a 2.5 μm Gaussian spot. This value is observed to be the threshold value for 5 μm liquid donor film using a 50 nm titanium metal absorber layer. The ink used in this study consists of an aqueous solution of glycerol (50% v/v) with Triton X-100 surfactant (1.4% v/v), a solution commonly employed in the literature [31, 32].

The delay between the lamp and the laser is adjusted to capture the snapshots of formed jet. This method has become popularized in the literature by many research groups in different studies [12, 24, 25, 20, 26]. Some studies also employ a second laser and a beam expander to light the system [10, 27, 28].

With a metal absorber, the required energy to create jet formation is lower than the BA-LIFT cases. The resulting images are given in Figure 1.3. Absorption of the laser into the titanium layer causes rapid heating which results in explosive boiling of the adjacent liquid and ejection of hot fragments of the metal film which can contaminate the ink [29, 11]. This produces a high pressure vapor cavity and drives the flow. Initial flow velocities are calculated around 200 m/s. In the fractured blister case, the ejection is propelled by the high-pressure gases discharged from the ruptured polyimide film. In this case, cavitation similar to the Titanium DRL leads to jet formation and the time-resolved images captured for this case look very similar (not shown here). The vapor cavity is observed to reach its maximum size in 1-2 μs. Because of the remnant momentum associated with the flow, the jet continues even after the cavity stops expanding. After the cavity collapses, it rebounds and undergoes a secondary expansion. This interesting phenomenon has been examined in literature [30].

Cavitation bubble collapse near a rigid boundary has long been studied [34, 35, 36] and one of the key characteristics of this scenario is the presence of a re-entrant jet. As

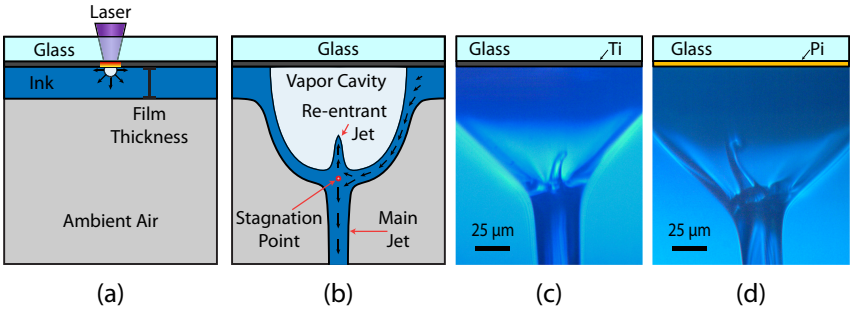


Figure 1.4 (a) Initial configuration of the problem (b) Schematic of the re-entrant jet with vapor cavity. Close-up experimental images acquired at 5 μs of gas cavities formed during the ejection of liquid from a 5-μm film using (c) titanium (11.8 μJ) and (d) polyimide (7.3 μJ) absorbing layers with a 2.5-μm beam. Internal re-entrant jets (directed upwards) are clearly visible within the gas cavity [33].

the bubble collapses, a secondary jet is initiated at the collapsing front and is directed toward the solid boundary. With high resolution imaging, we are able to observe the existence of a re-entrant jet during both the titanium DRL and the fractured polyimide blister case as shown in Figure 1.4.

In contrast, images from the BA-LIFT case with a not-ruptured blister are presented in Figure 1.5. In this case the jet formation mechanism is the rapid expansion of the blister as discussed above rather than cavitation and collapse. By controlling the laser fluence on the polyimide absorbing layer, it is possible to achieve blister expansion without fracture. There are no indications of cavitation within the liquid for the expanded blister actuated case. Instead, the ink on the expanding polyimide layer gains momentum which causes the fluid to develop into a jet. The jet initially propagates with a constant velocity of $\sim$25 m/s and the propagation is maintained due to the momentum of the jet, which pulls additional ink from the surrounding liquid film. As the jet extends from the film, the diameter at the base slightly increases and the diameter around the jet midpoint starts to decrease. This eventually results in the breaking up of the jet into spherical droplets because of the Rayleigh-Plateau instability [37, 38, 39].

1.4 Blister Formation

1.4.1 Dynamics of Blister Formation

Blister formation can be experimentally examined in detail by making use of time-resolved imaging and optical microscopy [16]. Blister expansion in time is shown in

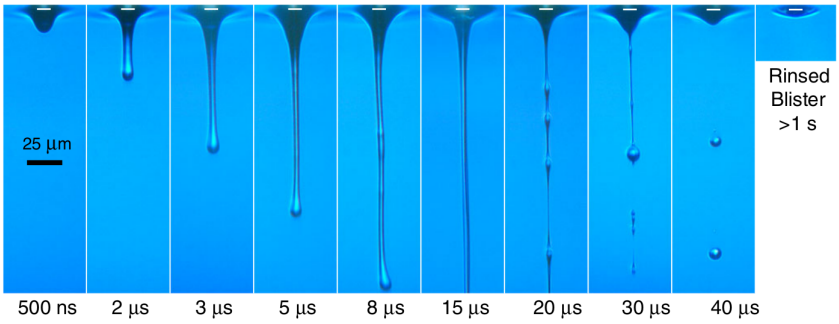
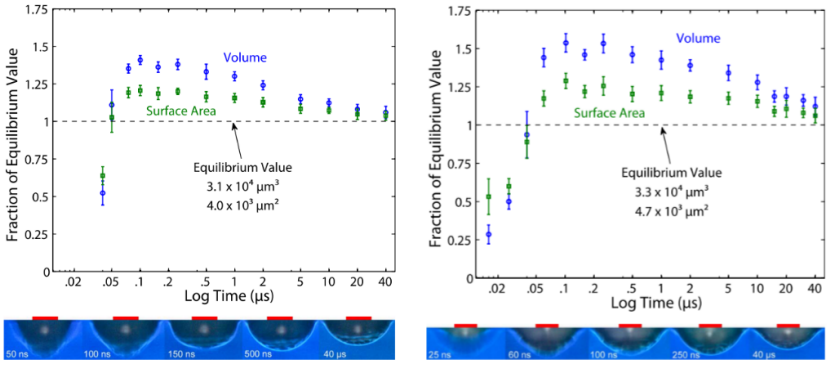


Figure 1.5 Time-resolved images of liquid jets expelled into the ambient air using an 7-μm expanded polyimide absorbing layer. A 2.7-μJ laser pulse is focused into the polyimide film to a spot size of 10 μm (indicated by a white marker), producing a rapidly expanding, sealed blister, which initiates liquid ejection from an adjacent 5-μm film. The vertical field of view is $\sim$200 μm. An image ($>$1 s) of the blister, rinsed of residual liquid, is shown for reference [12].



(a) (b)

Figure 1.6 (a) Time response of blisters formed on 3.5 μm thick polyimide film with a 20 μm top hat beam (2.6 J/cm^2). (b) Time response of blisters formed on 6 μm thick polyimide film with a 20 μm top hat beam (4.3 J/cm^2). In these cases, a 10 μm N-methyl-2-pyrrolidone (NMP) ink is used. (Top) Volume and surface area vs time. Error bars indicate $\pm$1 standard deviation in the values. (Bottom) Sample images of the blisters at several times. The bar indicates the 20 μm beam diameter

Table 1.1 Material properties used in the solution of the 1D heat equation [16].

	ρ (kg/m^3)	c_p (J/kg K)	k (W/m K)
Air	1.184	1012	0.025
Polyimide	1420	1089	0.15
Gas	25	1100	0.1
Glass	2500	879	0.94

Figure 1.6a for blisters formed on a 3.5 μm polyimide film with a 20 μm top hat beam at the fluence value of 2.6 J/cm^2. Similarly, Figure 1.6b shows the results for blisters formed on a 6 μm film with a 20 μm beam at 4.3 J/cm^2. Top plots present the volume and the exterior surface area given as a fraction of their equilibrium value with time. Here the equilibrium volume corresponds to the blister volume long after irradiation with the laser pulse. Bottom images represent blister expansion at various stages. Same trends, that are not reported here, are obtained also for a 10 μm beam diameter. Spot sizes given here are evaluated as the full width at 1/e^2. A side product of the laser ablation is plasma generation, which appears as white flashes in Figure 1.6.

The blister undergoes rapid expansion ($\sim$100 μs) under the effect of the pressurized trapped gases. As the blister expands, stresses in the film begin to build and the internal pressure drops due to the quenching of the gaseous products. Cooling of the products takes place because the blister volume is expanding [16]. Energy dissipates on the deforming polyimide, which results in the delamination of the thin film from the glass. At the ablation spot, the film delaminates from the substrate and when the pressure created by the gaseous products is no longer able to overcome the elastic stress in the film, blister acceleration ceases. After the blister reaches its peak, it starts to spring back and the total volume decreases. First by $\sim$150 ns, the internal pressure causes the sides of the blister to bow out, which makes the blister take a rather blunted shape. By $\sim$500 ns, the blister takes the more uniformly rounded shape. The expansion velocity for the 6 μm film case is calculated as $\sim$400-500 m/s, whereas for the 3.5 μm film the obtained velocity is $\sim$800-1200 m/s. This difference exists because a thicker film requires more energy to be dissipated into the stretching and bending as compared to a thinner film and it implies that film thickness should affect the ink ejection characteristics.

After the initial expansion of the blister, a gradual contraction is observed as depicted in Figure 1.6. This contraction continues for $\sim$50 μs. This contraction can be attributed to a further reduction in pressure caused by the cooling of the trapped gas. Heat equation is solved to evaluate the temperature of gaseous products with time. A simple examination can be performed by solving the heat equation in 1D. The equation is formulated as:

$$\rho c_p \frac{\partial T}{\partial t} = \frac{\partial}{\partial x}\left(k \frac{\partial T}{\partial x}\right) \tag{1.1}$$

which can be easily solved numerically. The required density (ρ), specific heat (c_p),

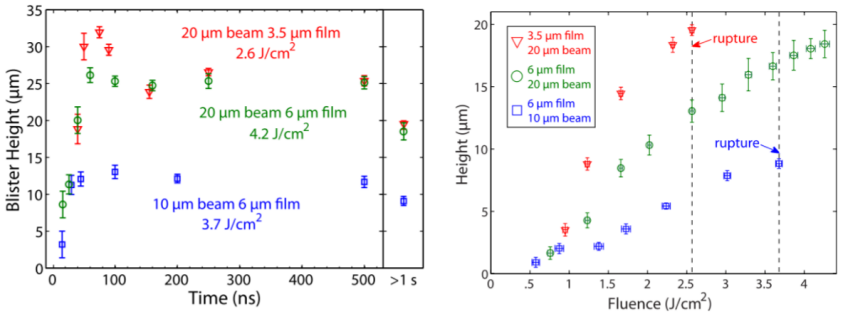


Figure 1.7 (a) Evolution of blister height during the initial period of rapid expansion. An overshoot and oscillation is visible in the blisters formed with a 20 μm beam. The effect is more pronounced with the thinner film. Steady-state blister heights are shown for reference. (b) Blister height vs laser fluence for different combinations of film thickness and beam size. The vertical dashed lines indicate the blister rupture flience for each case [16].

and thermal conductivity (k) values are given in Table 1.1. The gas density is approximated by assuming that the experimentally measured blister volume is filled with a mass of vapor equal to the estimated mass of ablated polyimide [21]. In this simple 1D model the blister is modeled as a 20 μm slab of gas, initially at the elevated temperature T_H and sandwiched between a semi-infinite domain of glass and a 3 μm layer of polyimide layer. The polyimide layer is in contact with ambient air which has a temperature of T_C. It is evaluated that the thermal decay has the same trend as the volume and surface area reduction. The results of this study show that the thermal decay takes place around the same time as the experimentally measured blister contraction, indicating that the cooling can be the reason for the observed phenomenon [16].

The evolution of blister height with time for different beam size, fluence, and film thickness values is given in Figure 1.7a. Blister size is crucial in determining the amount of ink to be ejected. It is important to understand how the blister size varies with changing parameters like film thickness, laser beam diameter, and fluence. This study shows that the blister height and width monotonically increase with increasing laser fluence above the ablation threshold of 0.1 J/cm^2 for 355 nm Nd:YAG lasers. The increase in height with fluence is given in Figure 1.7b. The reason for this increase in blister size is the increase in the mass of vaporized polyimide, increasing ablation depth (thereby thinning the remaining blister material) and the increase in the temperature of the trapped gaseous products [40]. Similarly, holding fluence constant and increasing the laser beam diameter produces a larger area over which the polyimide is vaporized and larger blister. For instance, it is observed that increasing the beam diameter from 10 to 20 μm results in nearly doubled blister heights.

The shape of the blisters reflect the relative contributions of stretching versus bend-

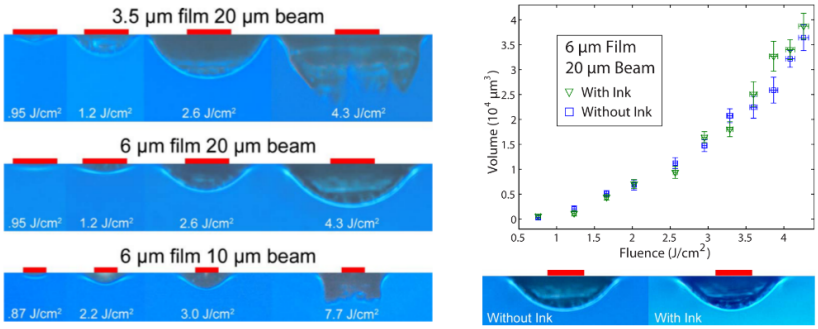


Figure 1.8 (a) Images of blisters formed at several fluences for different combinations of film thickness and beam size. The bars indicate the beam diameter (10 or 20 μm) (b) Blisters formed on 6 μm polyimide film with a 20 μm beam (4.3 J/cm^2) with and without a 10 μm liquid film of NMP. (Top) Blister volume as a function of fluence for blisters formed with and without an ink layer. Both curves overlap significantly indicating the minimal effect of the ink layer on the blister size. (Bottom) No noticeable difference in the shape between blisters formed with and without a liquid layer. The bars indicate the 20 μm beam diameter

ing stress as depicted in Figure 1.8a. When blister dimensions (width and height) are small relative to the film thickness, bending stresses dominate and the blister takes on a pointed shape. This is apparent in Figure 1.8a for 6 μm film with a 10 μm beam. As blister dimensions get larger, stretching becomes dominant [41]. This results in spherical cap blister shapes. An example case is shown in Figure 1.8 for 3.5 μm film with the 20 μm beam.

Blister formation under different energies are observed under optical microscope and secondary electron microscope (SEM) as presented in Figure 1.9. As noted before, when laser fluence exceeds the critical value, the rupture takes place and the blister opens like a flower [42]. However, such a regime is typically avoided in experiements to preserve the benefits of BA-LIFT in comparison to more traditional LIFT approaches.

1.4.2 Finite Element Modeling of Blister Formation

A modeling effort for the finite element simulation of blister deformation during the BA-LIFT process is given in [43]. This study captures initial expansion of the blister subject to the incident laser. The strain rates associated with the process are on the order of 10^5 to 10^7 s^{-1}, which makes the material properties given in data sheets not applicable. We resolved this issue by introducing a parameter mapping strategy that would account for temperature-depedent material properties. The strategy is forming a constant by bundling the material properties that vary with temperature together, and setting the value of this constant so that the numerically evaluated blister profile

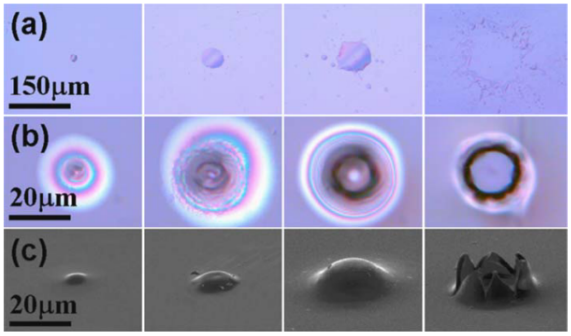


Figure 1.9 (a) Optical microscopy images of laser transferred droplets taken at 5, 7, 11, and 31 μJ from left to right. (b) Associated microscopy images of polyimide film. (c) SEM images of polyimide film taken at an angle of 70^o [14].

fits the experimentally observed blister shape. ANSYS Structural for finite element analysis (FEA) is used to implement the proposed model. The model in this study is developed using 7 μm blisters and verified on the formation of 3 μm blisters. Details of this process are elaborated below.

We begin with the Peirce equation to evaluate the dynamic flow stress:

$$\sigma_y = \sigma_{y0}\left(1 + \frac{\dot{\epsilon}_{pl}}{\gamma}\right)^m \tag{1.2}$$

where σ_{y0} is the static yield stress, γ is the material viscosity parameter, and m is the strain-rate-hardening parameter. These last two parameters are considered free fitting parameters and are determined using the parameter map analysis. The plastic strain rate ($\dot{\epsilon}_{pl}$) is calculated using the finite element software (in this case ANSYS). The driving force for the blister growth is the pressure change between the polymer layer and the glass substrate. The pressure change in between is formulated as:

$$P_t = P_{t-\Delta t}\left(\frac{V_{t-\Delta t}}{V_t}\right)^{\frac{c_p}{c_v}} + \eta\frac{1}{V_t}\int_{t-\Delta t}^{t} I(Fl,t)dt \tag{1.3}$$

which indicates the combination of an adiabatic increase and an increase due to the laser power. Here $I(Fl,t)$ is the instantaneous laser power and the integral extends over time. The functional form is Gaussian in time t, and the integral of this function over the entire pulse length is equal to the laser energy.

The second term on the right hand side of this equation is derived from the following formulas. We start with the simple relation that connects the temperature increase to the heat added:

$$\Delta T = \frac{\Delta Q}{mc_v} \tag{1.4}$$

where ΔQ is the heat added, m is the mass of the gas, and c_v is the specific heat at constant volume. The pressure change can be evaluated using the equation of state:

$$\Delta P = \frac{mR\Delta T}{MV} \tag{1.5}$$

where R is the universal gas constant, M is the molar mass of the gas, and V is its volume. Inserting (1.4) into (1.5) yields:

$$\Delta P = \frac{R\Delta Q}{MVc_v} \tag{1.6}$$

In this system the heat transfer takes place due to the laser, therefore, we need a formula for the energy deposited with the laser, so that the change in pressure can be expressed in terms of this deposited energy. The amount of laser energy converted into the thermal energy can be formulated as:

$$\Delta Q = k \int I(Fl, t)dt \tag{1.7}$$

where k is the conversion efficiency of laser energy to thermal energy in the gas. Inserting (1.7) into (1.6) yields:

$$\Delta P = \frac{kR}{Mc_v}\frac{1}{V}\int I(Fl, t)dt \tag{1.8}$$

It can be observed that this expression constitutes the second term on the right hand side of (1.3) with setting $\eta = kR/Mc_v$. During the fitting procedure η is varied to ensure that numerically evaluated blister heights match the experimentally observed blister heights. The correct selection of this parameter can be verified by comparing experimental and numerical results. This is shown in Figure 1.10 along with the calculated and measured blister shapes.

Time-dependent formation of the blister can be monitored experimentally and an empirical formula determined[15]. While the finite element model gives accurate results, an empirical formula for the blister formation is important if the focus is the jet formation dynamics. The inflated blister's shape is represented with a displacement function as:

$$\delta = X(r, E) \cdot T(t) \tag{1.9}$$

which is the product of a spatial component $X(r, E)$ and a temporal component $T(t)$. Here r denotes the radial coordinate, and E denotes the laser pulse energy. The spatial function represents the final shape of the blister as a function of laser energy. The temporal component is a normalized function that does not depend on laser energy. The spatial function has the form:

$$X(r, E) = H_0(E)\left(1 - \left(\frac{r}{R_0(E)}\right)^2\right)^C \tag{1.10}$$

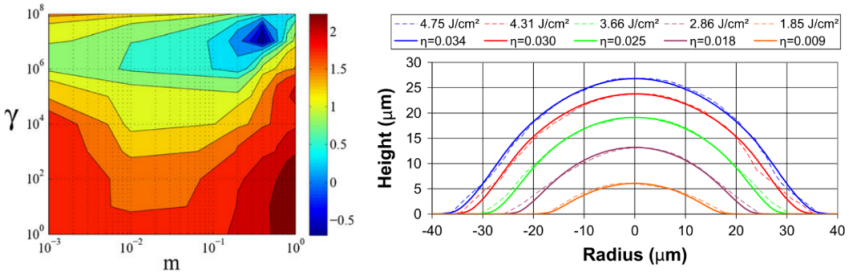


Figure 1.10 Left: Parameter map evaluated to find γ and m to evaluate the dynamic flow stress, σ_y, by choosing the values which yield the minimum average residual sum of squares (RSS). Right: The blister formation as evaluated via finite element simulations. The parameter η is varied to equate the numerically evaluated blister height to the experimental result [43]. Dashed lines determine the experimental profile whereas solid lines are the fitted blister profiles. [43]

where $H_0(E)$ is the blister height, $R_0(E)$ is the blister radius. Both of these parameters are functions of laser energy. The coefficient C depends whether the blister formation mechanism is stretching or bending. The two limiting cases are pure stretching ($C = 1$) and pure bending ($C = 2$). This expression is fit to each steady-state (500 ns) blister profile generated with different laser energies. It is found in [15] that C has an energy-independent average value of 1.25 ± 0.185 with blister height and radius fitted to the following functions:

$$H_0(E) = -0.0093E^2 + 2.5708E - 9.2618 \tag{1.11}$$

and

$$R_0(E) = 18.117\ln(E) - 12.887 \tag{1.12}$$

where values obtained from these expressions are in μm. It should be noted that this profile is fitted to blisters that are generated on a 7 μ m polyimide layer. The form of the function may change for different thickness values. The temporal function is the evolution of its blister height normalized by its steady-state value. It is observed from our experiments that the blister expands rapidly during the initial 50-100 ns and reaches a constant height within 150 - 250 ns. This behaviour is observed to be energy independent and we empirically determine the temporal function:

$$T(t) = \frac{2}{\pi} arctan(t/\tau) \tag{1.13}$$

where $\tau = 2.359 \times 10^{-8}$ s, and it is the time for the blister to reach 50% of its maximum height. This value is obtained by fitting the given form of the function onto the experimental data. Evolution of the temporal function and the change in steady state blister height with varying energy levels are given in Figure 1.11.

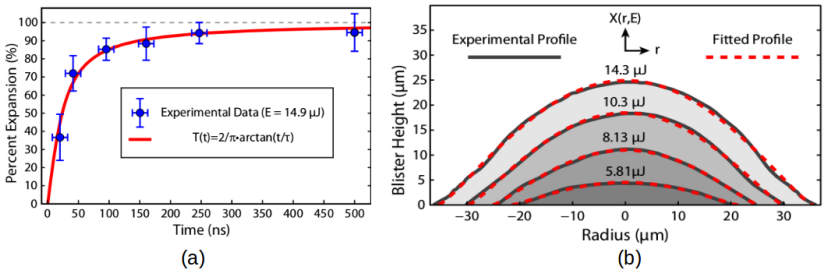


Figure 1.11 Results from the empirical formula for blister profile. (a) The normalized temporal evolution of blister height initiated with a 14.9 μJ laser pulse. Each data point represents the average of five measurements, and the vertical bars indicate ± 1 standard deviation. A fit is also shown on the plot. (b) Experimentally measured blister profiles (solid lines) shown with their associated fits (dashed lines) [15].

Equation (1.9) and the corresponding equations are very important as they describe the deforming solid boundary which leads to jet formation in the fluids. In the following sections, we use this as a as a boundary condition for fluid flow simulations.

1.5 Jet Formation and Expansion

The jet formation mechanism in BA-LIFT is the rapid mechanical deformation due to the expanding blister. This fact makes the process easier to simulate than traditional LIFT processes because the flow characteristics can be obtained without dealing with the complications associated with cavitation. That being said, some effort has been dedicated to model conventional LIFT processes. A recent example is [44], where the jet formation of a hydrogel layer under a Titanium DRL is simulated. An extension of this model to biomaterials is presented in [45]. Another approach for LIFT modeling is based on the two-temperature model to evaluate the temperature and stress levels during the absorption of the laser pulse [46, 27].

1.5.1 Computational Fluid Dynamics Model

Modeling of the BA-LIFT process, where the ejection mechanism is the rapid mechanical deformation of the solid boundary, is performed in [15]. The purpose of such numerical analysis is to develop a platform whereby parametric studies can be performed and optimum conditions can be evaluated for jet printing. The governing equations for the jet formation of Newtonian fluids during BA-LIFT are the well-known Navier-Stokes equations for incompressible flows with the addition of the

surface tension term. First, the continuity equation is expressed as:

$$\frac{\partial \rho}{\partial t} + \nabla \cdot (\rho \mathbf{u}) = 0 \tag{1.14}$$

The incompressibility condition is written as:

$$\nabla \cdot \mathbf{u} = 0 \tag{1.15}$$

The equation of motion:

$$\rho \left(\frac{\partial \mathbf{u}}{\partial t} + \mathbf{u} \cdot \nabla \mathbf{u} \right) = -\nabla p + \rho \mathbf{g} + \mu \nabla^2 \mathbf{u} + \gamma \kappa \delta_s \mathbf{n} \tag{1.16}$$

where ρ, $\mathbf{u}$, and μ are the density, velocity, and the dynamic viscosity, respectively. The last term in the equation given above is the contribution from surface tension, with γ denoting the surface tension coefficient, κ and $\mathbf{n}$ the curvature and normal vector to the interface. The Dirac delta function (δ_s) denotes that the surface tension term is applied only at the interface. The continuity equation is necessary in addition to the incompressibility condition because we are dealing with a two-phase flow (air and ink), and the numerical scheme solves for the fluid motion in two phases with different densities. Inserting the incompressibility equation into the continuity equation results in:

$$\frac{D\rho}{Dt} = 0 \tag{1.17}$$

which can be considered an advection equation for the fluid density.

In multi-phase flows, the interface can be represented in various ways. Two widely used techniques are the level-set method [47] and the volume-of-fluid (VOF) method [48]. Simulations that are presented with this chapter are performed using the VOF method because the mass is conserved intrinsically, and the topological changes are handled easily [49]. Within this scheme, the density can be defined as:

$$\rho(c) = c\rho_1 + (1 - c)\rho_2 \tag{1.18}$$

where ρ_1 and ρ_2 are the densities of the first and second fluids. The interface is represented implicitly with the volume-of-fluid method, which uses a volume fraction field $c(x, t)$ varying between 0 for a cell filled with the first phase (air) and 1 for the second phase (liquid). A phase dependent viscosity is defined similarly.

Boundary conditions are derived empirically from experiments. The deformation of the boundary is performed by imposing a boundary condition for blister deformation. These conditions are presented in Section 1.4.2. The time-dependent vertical velocity is specified as:

$$V_b(r, t, E) = \dot{h}_b = X(r, E)\dot{(}T)(t) = X(r, E)\frac{2/(\pi\tau)}{1 + (t/\tau)^2} \tag{1.19}$$

where the dots denote time derivatives and h_b, X, and T are defined in equations 1.10, 1.11, and 1.13.

The specific numerical scheme depends on the solver code used to perform simulations. Results presented in this chapter are obtained using Gerris [50] and CFD-ACE+ (ESI Group, Paris, France) (ESI CFD Inc. [51]). Compared to models previously developed for LIFT processes [44], the modeling of the BA-LIFT process does not include the solution of the energy equation because the energy absorption is limited to the interface between the polyimide layer and the glass substrate and has already been accounted for in equation 1.19. In addition, the low thermal conductivity of the polyimide makes it possible to neglect the heating of the ink during jet formation [11].

1.5.2 Effect of the Laser Energy

Parametric studies are performed in [15] to investigate the effects of ink properties on jet formation. The liquid layer investigated in this numerical study is NMP similar to the ink used in the experimental measurements of Figure 1.5. Properties of this liquid are taken as: μ = 1.7 mPa s, ρ = 1030 kg m^{-3}, γ = 40.79 mN m^{-1}. The ejections take place into a background of air (μ = 18.46 μPa s, ρ = 1.1614 kg m^{-3}).

The correlation between the simulation and experiments is presented with two cases given in Figure 1.12. This figure shows experimentally and numerically produced jets. Subfigures 1a and 1b show the close correspondence between experiment and numerical results for 5.4 μJ laser pulse. Subfigures 2a and 2b show the correspondence between results for a higher laser energy of 7.7 μJ. The configuration on the right shows the status of the jet at 8 μs with a glass acceptor surface 150 μm below the donor substrate. This close correspondence is significant considering that there are no additional free parameters included in simulations.

The quantitative correlation is also examined by comparing the transferred volume of ink between experiments and simulations. This comparison is presented in Figure 1.13, which focuses on a smaller range of laser energies near the threshold energy. This threshold laser energy, below which no fluid is transferred, is experimentally observed at 5.5 μJ. This value compares favorably with the threshold energy (5.115 μJ) predicted by the simulations. In the simulations, a second threshold energy is observed, below which all secondary droplets are reabsorbed by the ink film rather than transferred. Beyond threshold, both data sets exhibit a similar dependence on laser energy, with the simulated data points located well within the uncertainty of the experimental measurements. This validates the accuracy of the computational model in resolving the dependence of the ejection process process on laser energy input.

Different regimes of droplet formation during the process with changing energy are presented in Figure 1.14. The earlier time dynamics ($t \leq 300$ ns) of the jetting process follow the same qualitative trends with increasing energy, whereas the longer-time behavior differs. Below the threshold at 5.1 μJ, the jet's kinetic energy is insufficient for the droplet to detach from the ink film as shown in Figure 1.14a. Between 5.1 μJ and 5.115 μJ, a droplet is detached from the ink, but its velocity is in the direction of the liquid film. At the threshold, only 15 nJ higher than 5.1 μJ, the

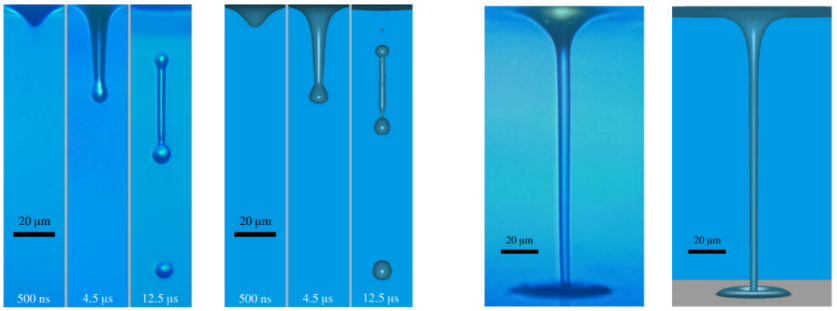


Figure 1.12 (1a) Experimentally acquired images and (1b) rendered computational results of fluid ejections from a 5 μm donor film of NMP using a 5.4 μJ laser pulse. The ejected fluid volume extracted from the last experimental image (1.2×10^{-15} m^3) compares favourably with that from the simulated ejection (1.0×10^{-15} m^3). Image frames are 134 μm high. (2a) Experimentally acquired image of a jet ejected from a 5 μm donor film of NMP acquired 8 μs after a 7.7 μJ laser pulse. The jet impacts with an acceptor substrate (glass slide) located 150 μm below the donor substrate. (2b) Rendered image of a simulated ejection at 8 μs corresponding to the experimental conditions. A 45^o contact angle is imposed at the acceptor–substrate boundary to match the experiment [15]

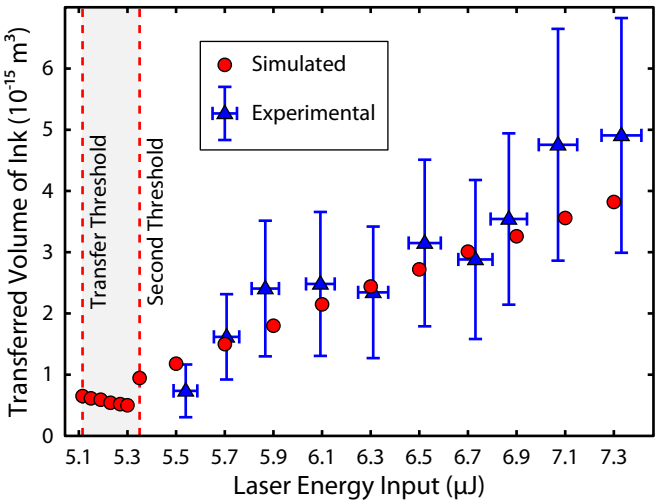


Figure 1.13 Plot of experimentally measured and simulated volumes of ink transferred as a function of laser energy. Each experimental data point represents the average of volumes measured from 10 transferred droplets, and the vertical error bars indicate ± 1 standard deviation. The horizontal error bars indicate ± 1 standard deviation in the shot-to-shot variation of laser energy.[15].

pinch-off of the droplet is observed at 8.5 μs. At this energy level, a smaller satellite droplet is observed to be forming. This satellite droplet has a velocity towards the ink film, and does not result in transfer (Figure 1.14b). It is important to notice that this energy level denotes a hard threshold, and 5.114 μJ energy does not result in the transfer of the droplet.

At this point it is useful to go back to Figure 1.13 and examine the change in transferred volume with energy. The jet formation is due to a phenomenon called Rayleigh-Plateau instability [39]. A general trend of the droplet formation through this instability is that the droplets produced scale with the jet diameter [52]. Between two thresholds (5.115 - 5.3 μJ), as laser energy is increased beyond the threshold, the jets become more elongated and narrower at their tip before the instability is initiated (Figure 1.13c). The satellite droplets obtain a velocity in the direction of the liquid film. These two effects combine to produce a decrease in transferred volume with increasing laser energy between thresholds.

However, beyond the second threshold, the satellite droplets are ejected with positive velocity. This results in a sharp increase in the ejected volume as depicted in Figure 1.13. Beyond the second threshold the deposited volume increases approximately linearly with laser energy. A case for higher laser energies (E = 6.1 μJ) is presented in Figure 1.14d with an acceptor surface. It is seen that the jet reaches the acceptor surface before pinch-off takes place.

1.5.3 Effect of the Ink Film Properties

For high resolution printing purposes, the narrow range of laser energies between two thresholds is ideal because this produces the smallest deposited volumes and minimizes the mechanical stress applied on the ink by the rapid blister formation. Therefore it is important to determine how this threshold regime changes as ink properties are varied. A parametric study is performed in [15] to investigate the effects of the ink properties on the threshold laser energy and transferred volume. The results of this study are presented in Figure 1.15. The other parameters of the ink are kept constant as the values of NMP while performing the parametric study.

Figure 1.15a shows that for film thicknesses smaller than 2.5 μm the threshold energy decreases with increasing film thickness. On the other hand, for thicknesses larger than 2.5 μm, the threshold laser energy increases linearly with increasing film thickness. This difference in the trend can be attributed to the competing factors during jet formation. For film thicknesses large compared to the blister width, the dependence on the film thickness is dominated by how much the initial impulse is transferred to the free surface. For example, the ratio of the initial free-surface velocity to the blister expansion velocity increases from 61% for a 10 μm film to 76% for a 5 μm film. With a 2.5 μm film, the two velocities are nearly equal. Here it is important to note that reducing film thickness enhances the influence of viscous stresses on the evolution of the flow. As the film thickness decreases, the boundary layer spans the film thickness in less time and the energy required to shear the liquid increases. At 2.5 μm film thickness the increase in viscous resistance offsets the im-

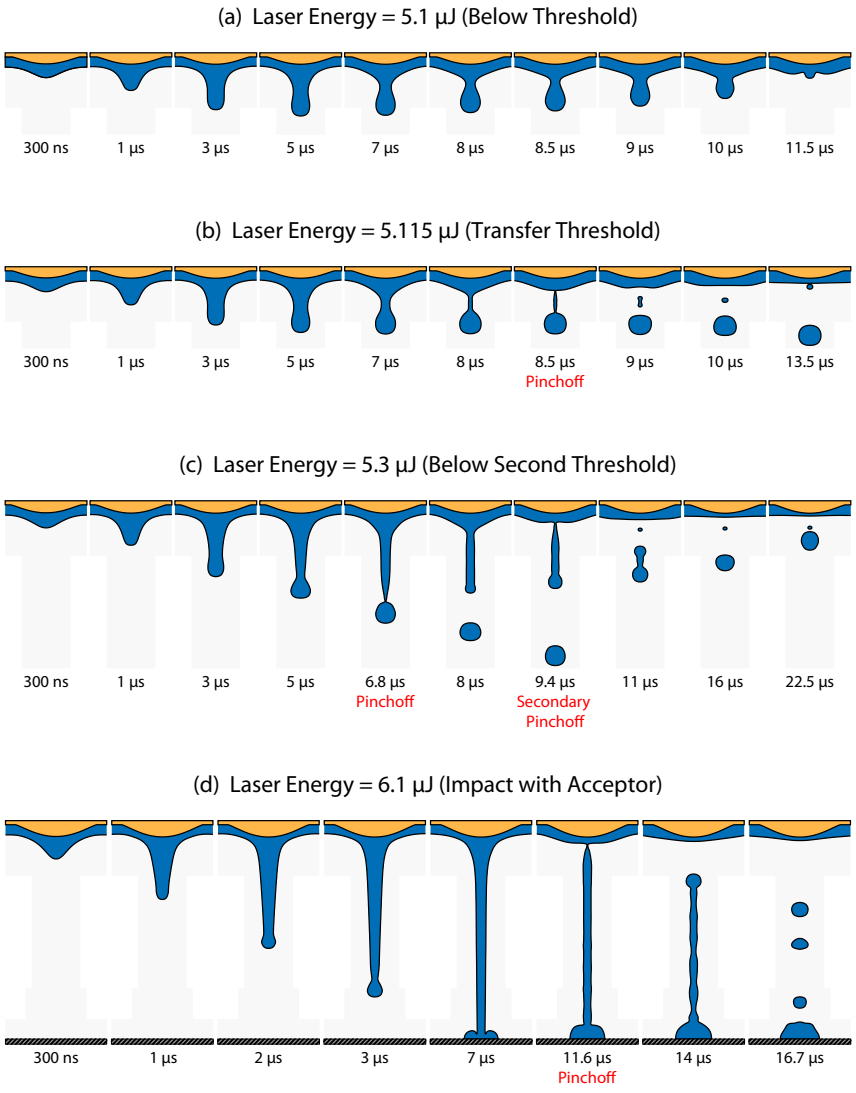


Figure 1.14 Simulation results for blister-actuated flows using standard ink properties initiated with laser energy inputs of: (a) E = 5.1 μJ (below threshold), (b) E = 5.115 μJ (transfer threshold) , (c) E = 5.3 μJ (below second threshold) (d) E = 6.1 μJ (impact with acceptor) [15].

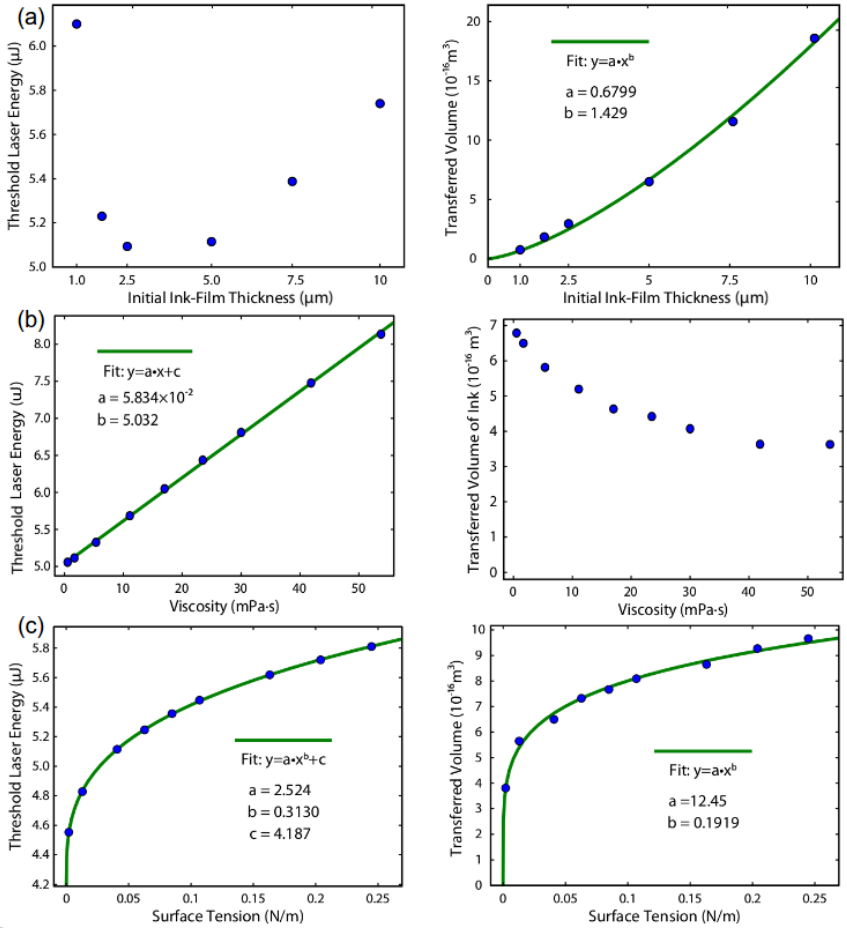


Figure 1.15 Results of the numerical parametric studies. Transferred volume and threshold energy values with varying parameters are presented [15].

provement to the coupling between the blister and the free surface, which results in a local minimum in the laser energy required for transfer.

Figure 1.15b shows the threshold laser energy increases with ink viscosity with a linear dependence. The mechanism for the linear relation between the threshold laser energy and viscosity is not currently understood, however the general increase in threshold energy versus viscosity is consistent with the additional energy required to induce jet formation. On the other hand, the volume transferred at this threshold decreases. This decrease can be attributed to the thinning in jet diameter with increasing viscosity.

Figure 1.15c shows that the laser energy input required for transfer increases with the surface tension, exhibiting a power-law behavior with an exponent of 0.3130. Also the volume transferred decreases with decreasing surface tension, suggesting that there would be no transfer if the surface tension could be reduced to zero. This leads to an optimization idea for high-resolution printing which utilizes the phenomenon that the surface tension of liquids decreases with increasing temperature. Using this trend, high resolution printing may be improved by heating.

The reasoning behind this power-law trend can be explained using the energy balance. Conservation of the total energy for the entire system can be written as:

$$\Delta E_T = \Delta E_k + \Delta E_s + \Delta E_d = 0 \tag{1.20}$$

where ΔE_k is the change in kinetic energy, ΔE_s is the change in surface energy, and ΔE_d is the energy dissipated by heat. This equation means that any decrease in kinetic energy is balanced by the increase in surface energy or dissipated heat. Here it is useful to examine how the kinetic energy changes with increasing laser beam energy. Kinetic energy of the fluid (remnant kinetic energy) can be evaluated as a function of increasing laser energy and it has been shown that the remnant kinetic energy scales as $E_k(t_0) \sim (E - E_{th})^{4.5}$, where E_{th} is the threshold energy for blister formation (not pinch-off) [53]. Using the same approach and defining $\bar{E} \equiv E - E_{th}$, the remnant kinetic energy scales with $E_k(t_0) \sim \bar{E}^{4.5}$. The surface tension results can be explained by observing that the same relation holds with the pinch-off energy ($\bar{E}_{th}$) and using $E_k(t_0) \sim \bar{E}^{4.5}$. Taking the conservation of energy formula given above into account, it can be said that the energy spent on the dissipation is very low because NMP has a low viscosity. Therefore we can assume that all the initial kinetic energy is converted to surface energy ($\Delta E_s = \gamma \Delta A$, where ΔA is the increase in surface area). This leads to the following relation between the remnant kinetic energy and the surface energy:

$$E_k(t_0) \sim \bar{E}_{th}^{4.5} \sim \gamma \Delta A \tag{1.21}$$

It is observed from simulation results in [53], that ΔA is relatively independent of $\bar{E}_{th}$, which implies that $\bar{E}_{th}^{4.5} \sim \gamma$. Solving for $\bar{E}_{th}$ yields:

$$\bar{E}_{th} \sim \gamma^{0.22} \tag{1.22}$$

which agrees with the measured exponent.

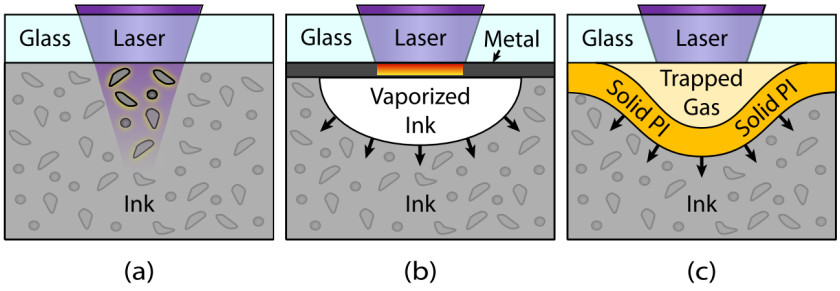


Figure 1.16 Variations of LIFT. (a) Absorption directly within the ink. (b) Laser absorption within a metal-film absorbing layer results in vaporization of the adjacent ink, producing a high-pressure vapor cavity. (c) Laser absorption within a polymer- film absorbing layer produces a rapidly expanding, sealed blister [33]

.

The effect of the ink density is not given in Figure 1.15 because its effect is negligible. Since the flow is modeled as incompressible and the boundary deformation is prescribed depending on the beam energy, the fluid's density has little influence on the velocity field that develops during blister's initial expansion. The influence of density is effective through the scaling of viscous (μ/ρ) and surface tension (γ/ρ) forces. This is verified by comparing simulation results in which the surface tension, viscosity and fluid densities are jointly varied by a factor of 1000. Both the jet length and its tip velocity differ by less than 0.4% at 2 μs.

1.6 Application to the Transfer of Delicate Materials

In the introduction of this chapter, we argued that BA-LIFT provides the ability to transfer materials without damaging their properties and we demonstrate this point on organic luminophores. Such materials will exhibit changes in their optical emission as well as chemical signatures when exposed to UV irradiation or excessive temperatures. In prior work [11], we compared the photoluminescence (PL) and nuclear magnetic resonance (NMR) spectra from different luminophores transferred using the three different LIFT techniques shown in Figure 1.16.

The transferred materials used in this study are blue 9-anthracenemethanol (AM), and a rather robust green tris(8-hydroxyquinoline)aluminum (Alq_3). These luminophores are added to the NMP, which has been employed in other studies as explained in previous sections, at a concentration of 30 mg/ml to form the inks without significantly affecting its rheological properties. The substrate used is glass for the direct laser absorption into the ink case. The donor substrate for the metal absorbing layer is glass slides with a 50 nm sputter-coated layer of titanium. The BA-LIFT process is performed with a 6 μm layer of polyimide. All the substrates

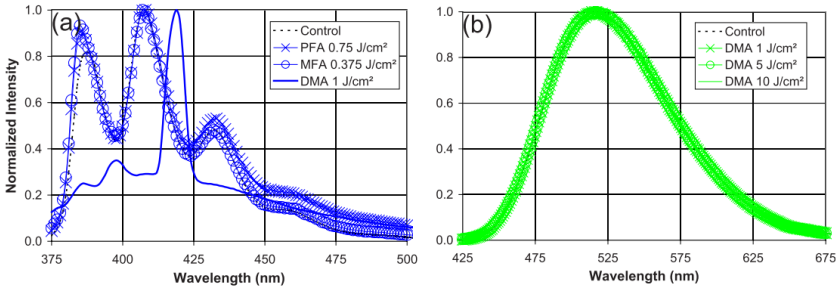


Figure 1.17 Photoluminescence spectra of (a) AM showing significant damage when printed via DMA (1 J/cm^2) but no apparent damage using either metal film absorber (MFA) (0.375 J/cm^2) or polymer film absorber (PFA or BA-LIFT) (0.75 J/cm^2). An undamaged spectrum of (b) Alq_3 material printed via DMA transferred at higher fluences can be seen for the Alq_3 molecule. [11].

are coated with a 10 μm thick ink using a wirecoater.

The material degradation is investigated by analyzing the printed droplets using each technique. Different fluence values are used to ensure similar droplet sizes for each technique. For photoluminescence studies, transferred material is washed off the acceptor surfaces using acetonitrile into quartz cuvettes. Results of the photoluminescence study are presented in Figure 1.17. Degradation is clearly apparent for AM that is deposited by direct matrix absorption as indicated by the modified peak structure in the spectrum. However Titanium DRL and BA-LIFT both show similar emission as the control sample. Conversely, the more robust Alq_3 does not appear affected by any of the LIFT conditions.

More detailed structural and chemical analysis is done with NMR studies, and again, the transfered materials are washed off, this time with 1/2 ml of deuterated acetone. Results of this study on AM are given in Figure 1.18. In the case of Alq_3 both PL results and NMR results show that there is no damage at the integrity of the transferred droplet. However, in the case of AM, there are clear indications of new peaks in the NMR spectrum corresponding to decompostion products created during the LIFT process. We see such peaks in the direct matrix absorption LIFT. In contrast to the PL measurements where the Titanium DRL showed no damage, the NMR clearly shows decomposition products in the transferred materials. Notably such peaks are not present in the BA-LIFT verifying the ability to transfer delicate materials without damage.

Additional studies have been performed on the optoelectronic properties of organic electronic device fabricated via BA-LIFT in addition to NMR and PL analyses. An example is presented in [13]. In this study, the fabrication of devices with ionic transition metal complexes (iTMCs) is performed using BA-LIFT. One of these devices is a tris(4,4'-di-tert-butyl-2,2'-bipyridyl)ruthenium, $[Ru(dtb-bpy)_3]^{2+}(PF_6^-)_2$ (Complex 1), electroluminescent device. Another sample is prepared using bis(5-trifluoromethyl,2-(2',4'-difluorophenyl)pyridyl), (4,4'-di-tert-butyl-2,2'-bipyridyl)

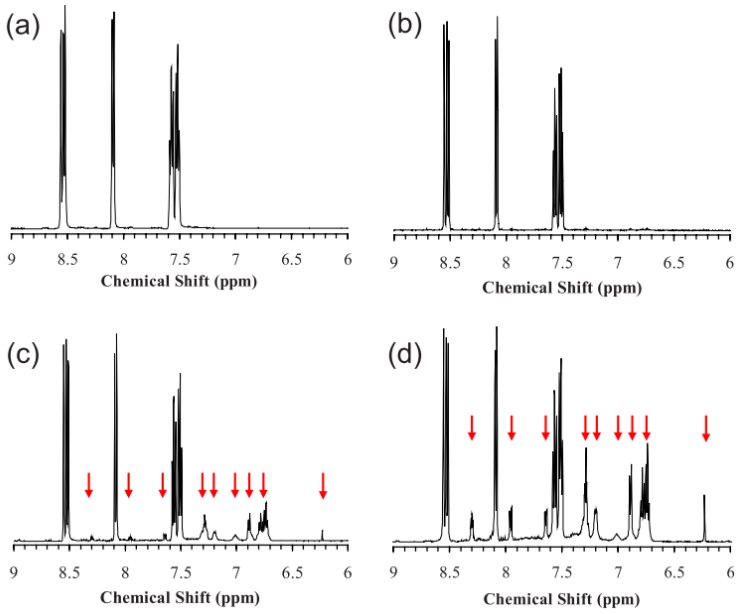


Figure 1.18 NMR spectra of AM for (a) control and printed using (b) BA-LIFT, (c) Titanium DRL, and (d) direct matrix absorption. Arrows indicate the degradation products present in corresponding techniques. No peaks exist in control or polymer absorptive layer [11].

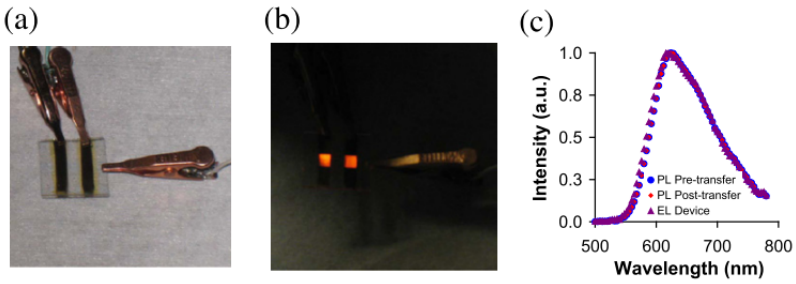


Figure 1.19 (a) Image of the LED (12.5 × 12.5 mm^2) under room light illumination. (b) Device operation under ambient conditions depicting two 2.5 × 2.5 mm^2 orange–red pixels. (c) Post-transfer PL and device EL match the pre-transfer solution PL [13].

iridium, $[Ir(F_5 - mppy)_2(dtb - bpy)](PF_6)$. Both of these samples are prepared according to the guidelines presented in literature [54, 55].

An image of the working device is given in Figure 1.19. It is seen that the pixels emit bright electroluminescence in ambient conditions under forward bias (Figure 1.19b). Uniformity of the electroluminescence is an indication that the integrity of the ITO layer is preserved during the BA-LIFT process, since damage would prevent the uniform charge transfer along the layer.

Photoluminescence measurements are performed with an Hg lamp and the emission spectra are recorded with a colorimeter. The emission spectrum of a Complex 1 film via photoluminescence (PL) is shown in 1.19c. It is seen that the PL spectrum of the BA-LIFT printed luminophore matches the non-printed control solution. Both curves also exhibit the same peak wavelength at 630 nm. This value is similar to those reported in literature [54, 56, 57]. Since both the shape and the peak wavelength of the curve match with the examples in the literature, properties of the molecule are not altered during the BA-LIFT process. Furthermore, similar results are observed for the devices fabricated in nitrogen environments via spin coating [54, 56]. Electrical performance of these devices are also evaluated and shown that the performance matches other devices in literature.

It is seen from these studies that polymer layer prevents damage to the ink, and device performance is not adversely affected.

1.7 Conclusions

In this chapter we have shown the underlying physics and applications of BA-LIFT, a technique developed as an alternative to conventional LIFT processes. BA-LIFT relies on the mechanical impulse created by an expanding blister to induce jet formation in a liquid or multiphase ink. Since the incident laser energy is absorbed in a shallow region of the thick polymer film, the associated blister maintains thermal

and optical insulation between the laser and the ink. Expansion of the blister is investigated through time-resolved imaging and the underlying physics is examined using finite element simulations. Also empirical blister formation formulas are derived from time-resolved images, which are used as boundary condition for analytical and computational studies performed to examine the jet formation.

Time-resolved images and developed CFD models can provide detail on the jet formation process and shed light on the importance of different parameters on the transfer process. Parametric studies are performed to investigate jet properties at different transfer regimes and provide users with a greater understanding of how to control the process to optimize the transfer. Most notably, BA-LIFT is demonstrated to be a suitable technique for the transfer of sensitive materials, since it prevents degradation and damage to chemically, thermally, or optically delicate materials.

References

1 Adrian, F., Bohandy, J., Kim, B., Jette, A.N., and Thompson, P. (1987) A study of the mechanism of metal deposition by the laser-induced forward transfer process. *Journal of Vacuum Science & Technology B*, **5** (5), 1490–1494.

2 Esrom, H., Zhang, J.Y., Kogelschatz, U., and Pedraza, A.J. (1995) New approach of a laser-induced forward transfer for deposition of patterned thin metal films. *Applied Surface Science*, **86** (1), 202–207.

3 Serra, P., Colina, M., Fernández-Pradas, J.M., Sevilla, L., and Morenza, J.L. (2004) Preparation of functional DNA microarrays through laser-induced forward transfer. *Applied Physics Letters*, **85** (9), 1639–1641.

4 Hopp, B., Smausz, T., Antal, Z., Kresz, N., Bor, Z., and Chrisey, D. (2004) Absorbing film assisted laser induced forward transfer of fungi (trichoderma conidia). *Journal of Applied Physics*, **96**, 3478–3481.

5 Hopp, B., Smausz, T., Kresz, N., Barna, N., Bor, Z., Kolozsvári, L., Chrisey, D.B., Szabó, A., and Nógrádi, A. (2005) Survival and proliferative ability of various living cell types after laser-induced forward transfer. *Tissue Engineering*, **11** (11-12), 1817–1823.

6 Colina, M., Serra, P., Fernández-Pradas, J.M., Sevilla, L., and Morenza, J.L. (2005) Dna deposition through laser induced forward transfer. *Biosensors and Bioelectronics*, **20** (8), 1638–1642.

7 Schultze, V. and Wagner, M. (1991) Laser-induced forward transfer of aluminium. *Applied Surface Science*, **52** (4), 303–309.

8 Banks, D.P., Grivas, C., Mills, J.D., Eason, R.W., and Zergioti, I. (2006) Nano-droplets deposited in microarrays by femtosecond ti: sapphire laser-induced forward transfer. *Applied Physics Letters*, **89** (193107), 1–3.

9 Yamada, H., Sano, T., Nakayama, T., and Miyamoto, I. (2002) Optimization of laser-induced forward transfer process of metal thin films. *Applied Surface Science*, **197**, 411–415.

10 Boutopoulos, C., Kalpyris, I., Serpetzoglou, E., and Zergioti, I. (2014) Laser-induced forward transfer of silver nanoparticle ink: time-resolved imaging of the jetting dynamics and correlation with the printing quality. *Microfluidics and Nanofluidics*, **16** (3), 493–500.

11 Kattamis, N.T., McDaniel, N.D., Bernhard, S., and Arnold, C.B. (2009) Laser direct write printing of sensitive and robust light emitting organic molecules. *Applied Physics Letters*, **94** (103306), 1–3.

12 Brown, M.S., Kattamis, N.T., and Arnold, C.B. (2011) Time-resolved dynamics of laser-induced micro-jets from thin liquid films. *Microfluidics and Nanofluidics*, **11** (2), 199–207.

13 Kattamis, N.T., McDaniel, N.D., Bernhard, S., and Arnold, C.B. (2011) Ambient laser direct-write printing of a patterned organo-metallic electroluminescent device. *Organic Electronics*, **12** (7), 1152–1158.

14 Kattamis, N.T., Purnick, P.E., Weiss, R., and Arnold, C.B. (2007) Thick film laser induced forward transfer for deposition of thermally and mechanically sensitive materials. *Applied Physics Letters*, **91** (171120), 1–3.

15 Brown, M.S., Brasz, C.F., Ventikos, Y., and Arnold, C.B. (2012) Impulsively actuated jets from thin liquid films for

high-resolution printing applications. *Journal of Fluid Mechanics*, **709**, 341–370.

16 Brown, M.S., Kattamis, N.T., and Arnold, C.B. (2010) Time-resolved study of polyimide absorption layers for blister-actuated laser-induced forward transfer. *Journal of Applied Physics*, **107** (083103), 1–8.

17 Urech, L. and Lippert, T. (2010) Photoablation of Polymer Materials, in *Photochemistry and Photophysics of Polymer Materials* (ed. N. S. Allen), John Wiley & Sons, Inc., Hoboken, NJ, USA, pp. 541–568, doi:10.1002/9780470594179.ch14.

18 Lippert, T., Hauer, M., Phipps, C.R., and Wokaun, a. (2003) Fundamentals and applications of polymers designed for laser ablation. *Applied Physics A: Materials Science & Processing*, **77**, 259–264, doi:10.1007/s00339-003-2111-y.

19 Lippert, T. (2010) UV Laser Ablation of Polymers: From Structuring to Thin Film Deposition, in *Laser-Surface Interactions for New Materials Production*, pp. 141–175, doi:10.1007/978-3-642-03307-0_7.

20 Brasz, C.F., Yang, J.H., and Arnold, C.B. (2015) Tilting of adjacent laser-induced liquid jets. *Microfluidics and Nanofluidics*, **18** (2), 185–197.

21 Brannon, J.H., Lankard, J., Baise, A., Burns, F., and Kaufman, J. (1985) Excimer laser etching of polyimide. *Journal of Applied Physics*, **58** (5), 2036–2043.

22 Ortelli, E.E., Geiger, F., Lippert, T., Wei, J., and Wokaun, A. (2000) UV-Laser-Induced Decomposition of Kapton Studied by Infrared Spectroscopy. *Macromolecules*, **33** (14), 5090–5097.

23 Dwivedi, A. (2007) Recent advances in pulsed laser ablated plasma plumes: A review. *Surface Review and Letters*, **14** (01), 57–69.

24 Feinaeugle, M., Alloncle, A., Delaporte, P., Sones, C., and Eason, R. (2012) Time-resolved shadowgraph imaging of femtosecond laser-induced forward transfer of solid materials. *Applied Surface Science*, **258** (22), 8475–8483.

25 Biver, E., Rapp, L., Alloncle, A.P., Serra, P., and Delaporte, P. (2014) High-speed multi-jets printing using laser forward transfer: time-resolved study of the ejection dynamics. *Optics Express*, **22** (14), 17 122–17 134.

26 Puerto, D., Biver, E., Alloncle, A.P., and Delaporte, P. (2016) Single step high-speed printing of continuous silver lines by laser-induced forward transfer. *Applied Surface Science*, **374**, 183–189.

27 Pohl, R., Visser, C.W., Römer, G.W., Lohse, D., Sun, C., Huis, B. *et al.* (2015) Ejection regimes in picosecond laser-induced forward transfer of metals. *Physical Review Applied*, **3** (024001), 1–9.

28 Desrus, H., Chassagne, B., Catros, S., Artigues, C., Devillard, R., Petit, S., Deloison, F., Frricain, J., Guillemot, F., and Kling, R. (2016) Laser assisted bioprinting using a femtosecond laser with and without a gold transductive layer: a parametric study, in *SPIE BiOS*, International Society for Optics and Photonics, 970600, pp. 1–18.

29 Smausz, T., Hopp, B., Kecskemeti, G., and Bor, Z. (2006) Study on metal microparticle content of the material transferred with absorbing film assisted laser induced forward transfer when using silver absorbing layer. *Applied Surface Science*, **252** (13), 4738–4742.

30 Akhatov, I., Lindau, O., Topolnikov, A., Mettin, R., Vakhitova, N., and Lauterborn, W. (2001) Collapse and rebound of a laser-induced cavitation bubble. *Physics of Fluids (1994-present)*, **13** (10), 2805–2819.

31 Colina, M., Duocastella, M., Fernández-Pradas, J.M., Serra, P., and Morenza, J.L. (2006) Laser-induced forward transfer of liquids: Study of the droplet ejection process. *Journal of Applied Physics*, **99** (084909), 1–7.

32 Duocastella, M., Fernández-Pradas, J., Serra, P., and Morenza, J. (2008) Jet formation in the laser forward transfer of liquids. *Applied Physics A*, **93** (2), 453–456.

33 Brown, M.S. (2011) *Experimental and Numerical Study of Laser-Induced Forward Transfer Printing of Liquids*, Ph.D. thesis, PRINCETON UNIVERSITY.

34 Benjamin, T.B. and Ellis, A.T. (1966) The collapse of cavitation bubbles and the pressures thereby produced against solid boundaries. *Philosophical Transactions of the Royal Society of London A: Mathematical, Physical and Engineering*

Sciences, **260** (1110), 221–240.

35 Plesset, M.S. and Chapman, R.B. (1971) Collapse of an initially spherical vapour cavity in the neighbourhood of a solid boundary. *Journal of Fluid Mechanics*, **47** (2), 283–290.

36 Blake, J.R. and Gibson, D. (1987) Cavitation bubbles near boundaries. *Annual Review of Fluid Mechanics*, **19** (1), 99–123.

37 Plateau, J.A.F. (1873) *Statique expérimentale et théorique des liquides soumis aux seules forces moléculaires*, vol. 2, Gauthier-Villars.

38 Strutt, J.W. and Rayleigh, L. (1878) On the instability of jets. *Proc. London Math. Soc*, **10** (4).

39 Eggers, J. (1997) Nonlinear dynamics and breakup of free-surface flows. *Reviews of Modern Physics*, **69** (3), 865–929.

40 Dreyfus, R. (1992) Cn temperatures above laser ablated polyimide. *Applied Physics A*, **55** (4), 335–339.

41 Arjun, A. and Wan, K.T. (2005) Derivation of the strain energy release rate g from first principles for the pressurized blister test. *International journal of adhesion and adhesives*, **25** (1), 13–18.

42 Gu, J., Tay, E., Lim, P., and Lim, P. (2002) Micro-humps formed in excimer laser ablation of polyimide using mask projection system. *Applied Physics A*, **74** (4), 487–491.

43 Kattamis, N.T., Brown, M.S., and Arnold, C.B. (2011) Finite element analysis of blister formation in laser-induced forward transfer. *Journal of Materials Research*, **26** (18), 2438–2449.

44 Mézel, C., Hallo, L., Souquet, A., Breil, J., Hébert, D., and Guillemot, F. (2009) Self-consistent modeling of jet formation process in the nanosecond laser pulse regime. *Physics of Plasmas (1994-present)*, **16** (123112), 1–7.

45 Mézel, C., Souquet, A., Hallo, L., and Guillemot, F. (2010) Bioprinting by laser-induced forward transfer for tissue engineering applications: jet formation modeling. *Biofabrication*, **2** (1), 014 103.

46 Shugaev, M.V. and Bulgakova, N.M. (2010) Thermodynamic and stress analysis of laser-induced forward transfer of metals. *Applied Physics A*, **101** (1), 103–109.

47 Sethian, J.A. (1996) A fast marching level set method for monotonically advancing fronts. *Proceedings of the National Academy of Sciences*, **93** (4), 1591–1595.

48 Hirt, C.W. and Nichols, B.D. (1981) Volume of fluid (VOF) method for the dynamics of free boundaries. *Journal of Computational Physics*, **39** (1), 201–225.

49 Kleefsman, K., Fekken, G., Veldman, A., Iwanowski, B., and Buchner, B. (2005) A volume-of-fluid based simulation method for wave impact problems. *Journal of Computational Physics*, **206** (1), 363–393.

50 Popinet, S. (2003) Gerris: a tree-based adaptive solver for the incompressible euler equations in complex geometries. *Journal of Computational Physics*, **190** (2), 572–600.

51 Group, E. *et al.*, Cfd-ace+.

52 Teng, H., Kinoshita, C., and Masutani, S. (1995) Prediction of droplet size from the breakup of cylindrical liquid jets. *International Journal of Multiphase Flow*, **21** (1), 129–136.

53 Brasz, C.F., Arnold, C.B., Stone, H.A., and Lister, J.R. (2015) Early-time free-surface flow driven by a deforming boundary. *Journal of Fluid Mechanics*, **767**, 811–841.

54 Bernhard, S., Barron, J.A., Houston, P.L., Abruna, H.D., Ruglovksy, J.L., Gao, X., and Malliaras, G.G. (2002) Electroluminescence in ruthenium (ii) complexes. *Journal of the American Chemical Society*, **124** (45), 13 624–13 628.

55 Slinker, J.D., Koh, C.Y., Malliaras, G.G., Lowry, M.S., and Bernhard, S. (2005) Green electroluminescence from an ionic iridium complex. *Applied Physics Letters*, **86** (17), 173 506–173 506.

56 Handy, E.S., Pal, A.J., and Rubner, M.F. (1999) Solid-state light-emitting devices based on the tris-chelated ruthenium (ii) complex. 2. tris (bipyridyl) ruthenium (ii) as a high-brightness emitter. *Journal of the American Chemical Society*, **121** (14), 3525–3528.

57 Balzani, V., Barigelletti, F., and De Cola, L. (1990) Metal complexes as light absorption and light emission sensitizers, in *Photoinduced Electron Transfer II*, Springer, pp. 31–71.